Research Square

Preprints are preliminary reports that have not undergone peer review.
They should not be considered conclusive, used to inform clinical practice,
or referenced by the media as validated information.

# A Block Hybrid Compact Finite Difference Scheme for Nonlinear Volterra Partial Integro-Differential Equations

**Phumlani Dlamini**

pgdlamini@uj.ac.za

University of Johannesburg

**James Malele**

University of Johannesburg

**Simphiwe Simelane**

University of Johannesburg

**Research Article**

**Keywords:**

**Posted Date:** May 25th, 2026

**DOI:** https://doi.org/10.21203/rs.3.rs-9655680/v1

**License:** This work is licensed under a Creative Commons Attribution 4.0 International License.
Read Full License

**Additional Declarations:** No competing interests reported.

# A Block Hybrid Compact Finite Difference Scheme for Nonlinear Volterra Partial Integro-Differential Equations

Phumlani Dlamini*, James Malele, and Simphiwe Simelane

Department of Mathematics and Applied Mathematics, University of Johannesburg, P.O. Box 17011, Doornfontein, Johannesburg 2028, South Africa

May 12, 2026

**Abstract**

This paper presents a highly accurate numerical framework for solving nonlinear parabolic and second-order Volterra partial integro-differential equations (PIDEs) with memory effects. The method is based on the Method of Lines (MOL), where spatial discretization is performed using a sixth-order implicit compact finite difference (CFD) scheme, providing high accuracy on relatively coarse grids. The resulting system of ordinary integro-differential equations is integrated using a block hybrid method (BHM) constructed via the collocation principle. Unlike traditional multistep methods, the BHM computes multiple intra-step values simultaneously, yielding a self-starting and high-order stable temporal scheme. A key contribution is the development of a consistent quadrature marching strategy for the Volterra integral term that employs the same Lagrange polynomial basis as the temporal discretization, thereby preserving the global sixth-order convergence of the method. The resulting nonlinear algebraic systems are solved using Newton's method. Numerical experiments involving nonlinear kernels and exponential nonlinearities demonstrate the high accuracy and efficiency of the proposed CFD–BHM framework, achieving low maximum absolute errors, outperforming several existing methods reported in the literature.

## 1 Introduction

Partial integro-differential equations (PIDEs) serve as vital mathematical models in numerous scientific and engineering disciplines, including fluid mechanics, biological population dynamics, and heat conduction [1]. While standard partial differential equations (PDEs) are effective at modeling local interactions in space and time, they often fail to capture the behavior of systems where the current state is influenced by its past history. This phenomenon, known as the "memory effect," necessitates the inclusion of an integral term in the basic differential formulation to represent systems with delayed or distributed responses [2, 3].

In particular, parabolic Volterra PIDEs are essential for representing physical situations such as the compression of viscoelastic media, nuclear reactor dynamics, and reaction-diffusion processes [4, 5]. Because these equations frequently involve nonlinear kernels and complex boundary conditions, finding exact analytical solutions is generally impossible. Consequently, the development of accurate, stable, and computationally efficient numerical methods has become a highly significant area of research [6].

*Corresponding author. E-mail: pgdlamini@uj.ac.za

To achieve high-order spatial accuracy, the compact finite difference (CFD) method has emerged as a powerful alternative to traditional approaches [7, 8, 9]. Unlike conventional finite difference schemes that require increasingly large stencils to achieve higher precision, compact schemes are implicit in nature, relating the derivative values at neighboring grid points to the function values themselves [10]. This implicit formulation provides a "spectral-like" resolution capable of capturing small-scale features and high-frequency oscillations more effectively than explicit schemes of the same order [11]. While pseudospectral methods are often cited for their exponential convergence rates, they are frequently limited by complex geometries and specific boundary conditions. In contrast, CFD schemes offer greater flexibility for application to diverse physical domains and can maintain fourth- or sixth-order accuracy on relatively coarse grids, significantly improving computational efficiency and reducing memory overhead [12, 13].

However, achieving high-order spatial resolution is only one part of the challenge; the temporal evolution and the cumulative nature of the Volterra integral term demand an equally sophisticated integration strategy. A significant advancement in the numerical treatment of time-dependent problems is the development of block hybrid methods (BHMs) [14]. These methods bridge the gap between traditional linear multi-step methods and single-step approaches by solving for multiple solution values simultaneously within a single computational block [15]. By strategically introducing intra-step or off-grid points, BHMs are able to circumvent the zero-stability limitations traditionally imposed by the Dahlquist barrier, permitting the construction of numerical schemes with significantly higher orders of accuracy than standard methods [16]. A primary structural advantage of the BHM framework is its self-starting nature; unlike conventional multi-step methods, BHMs do not require external starting values or complex predictor-corrector subroutines, which greatly simplifies implementation and minimizes computational costs [17].

The precision and versatility of BHMs have been further enhanced through the strategic selection of optimal points and integration with linearization schemes. For instance, utilizing points derived from the roots of the first derivative of shifted Legendre polynomials has allowed for numerical orders of convergence exceeding seven [18]. Furthermore, by coupling BHMs with Quasilinearization Methods (QLM) or the Simple Iteration Method (SIM), researchers have successfully solved highly complex nonlinear evolution equations and sensitive chaotic systems with minimal residual errors [15, 19].

Despite the breadth of existing literature on CFD and BHM independently, there remains a critical need for a unified numerical framework that balances the spectral-like spatial precision of compact schemes with the high-order temporal stability of block hybrid methods, specifically for the solution of Volterra PIDEs. The integration of these two methodologies offers a promising path toward resolving the memory-dependent behavior of these systems without the prohibitive computational costs of traditional global methods. In this paper, we aim to develop a robust and unified numerical framework that integrates sixth-order compact finite difference schemes for spatial discretization with high-order block hybrid methods for temporal evolution, specifically designed to solve nonlinear parabolic Volterra PIDEs. By coupling these two high-precision methodologies, we address the computational bottlenecks associated with history-dependent terms and nonlinear kernels. Through a series of rigorous numerical experiments, we demonstrate that the proposed CFD-BHM framework achieves sixth-order convergence in both space and time, maintains exceptional stability for stiff problems, and yields significantly higher accuracy with fewer grid points compared to existing methods in the literature.

## 2 Numerical Approach: The Method of Lines

In this work, we apply the block hybrid and compact finite difference method to solve one-dimensional partial integro-differential equations (PIDEs):

$$\frac{\partial w}{\partial t} = \alpha(x,t)\frac{\partial^2 w}{\partial x^2} + \int_0^t K(x,t,s,w(x,s))\,ds + g(x,t), \quad x \in [a,b],\, t \in [0,T], \tag{1}$$

with the following initial and boundary conditions:

$$\begin{aligned} &w(x,0) = \phi(x), \quad x \in [a,b], \\ &w(a,t) = h(t), \quad w(b,t) = l(t), \quad t \in [0,T], \end{aligned} \tag{2}$$

where $\alpha(x,t)$ represents the diffusion coefficient, $g(x,t)$ is the source term, and the integral operator captures the historical dependencies of the system through a potentially nonlinear kernel function $K$ [20, 4].

The core strategy is the method of lines. The spatial dimension is discretized first, transforming the single PIDE into a large system of coupled ordinary integro-differential equations (IDEs) in time. Let the spatial domain $[a,b]$ be discretized using a uniform grid defined by $x_i = a + ih$ for $i = 0, 1, \ldots, N$, where $h = (b-a)/N$ is the step size. Let $\boldsymbol{W}(t) \in \mathbb{R}^{N-1}$ be the vector of unknown function values at the interior grid points:

$$\boldsymbol{W}(t) = [w(x_1,t), w(x_2,t), \ldots, w(x_{N-1},t)]^T \tag{3}$$

The semi-discretized system can be written abstractly as:

$$\frac{d\boldsymbol{W}}{dt} = \boldsymbol{G}(t, \boldsymbol{W}(t)) \tag{4}$$

where $\boldsymbol{G}$ is a vector function representing the discretized right-hand side of Equation (1).

## 3 Spatial Discretization: Compact Finite Differences

To approximate the second spatial derivative $\frac{\partial^2 w}{\partial x^2}$ with high accuracy, a sixth-order compact finite difference (CFD) scheme is employed. Unlike standard explicit stencils, a CFD scheme defines an implicit relationship between the function values and its derivatives. For the second derivative, this relationship takes the matrix form:

$$\boldsymbol{A}\boldsymbol{w}'' \approx \frac{1}{h^2}\boldsymbol{B}\boldsymbol{w} \tag{5}$$

where $\boldsymbol{w}$ is the vector of function values at all grid points, $\boldsymbol{w}''$ is the vector of second derivatives, and $\boldsymbol{A}$ and $\boldsymbol{B}$ are banded matrices defined by the scheme's stencils.

### 3.1 Derivation of Sixth-Order CFD Schemes

The specific stencils used to populate the $\boldsymbol{A}$ and $\boldsymbol{B}$ matrices are derived as follows.

#### 3.1.1 Interior Point Schemes

For interior grid points ($i = 2, \ldots, N-2$), a symmetric scheme for the second derivative is derived from the general form:

$$\beta w''_{i-1} + w''_i + \beta w''_{i+1} = \frac{c}{h^2}(w_{i+1} - 2w_i + w_{i-1}) + \frac{d}{h^2}(w_{i+2} - 2w_i + w_{i-2}) \tag{6}$$

By matching Taylor series expansions, the unique coefficients for a sixth-order scheme are found:

$$\beta = \frac{2}{11}, \quad c = \frac{12}{11}, \quad d = \frac{3}{44}$$

This results in the explicit sixth-order compact scheme implemented in the code:

$$\begin{aligned} \frac{2}{11}w''_{i-1} + w''_i + \frac{2}{11}w''_{i+1} = &\frac{12}{11h^2}(w_{i+1} - 2w_i + w_{i-1}) \\ &+ \frac{3}{44h^2}(w_{i+2} - 2w_i + w_{i-2}) \end{aligned} \tag{7}$$

with truncation error:

$$\tau_i = -\frac{23}{55440}h^6 w_i^{(8)} \tag{8}$$

### 3.1.2 Boundary Schemes

To preserve sixth-order accuracy throughout the domain, the interior compact finite difference schemes must be complemented by appropriately constructed boundary closures. Because the second derivative is a symmetric operator, the right boundary closures are obtained by symmetry from the left boundary schemes. The following four boundary stencils are used in the implementation.

**Scheme at the Left Boundary ($i = 0$)**

$$w''_0 + \frac{126}{11}w''_1 = \frac{1}{h^2}\left(\frac{13097}{990}w_0 - \frac{2943}{110}w_1 + \frac{573}{44}w_2 + \frac{167}{99}w_3 - \frac{18}{11}w_4 + \frac{57}{110}w_5 - \frac{131}{1980}w_6\right). \tag{9}$$

where the leading truncation error is:

$$\tau_0 = \frac{339}{6160}h^6 w_0^{(8)} \tag{10}$$

**Scheme near the Left Boundary ($i = 1$ )**

$$\frac{11}{128}w''_0 + w''_1 + \frac{11}{128}w''_2 = \frac{1}{h^2}\left(\frac{585}{512}w_0 - \frac{141}{64}w_1 + \frac{459}{512}w_2 + \frac{9}{32}w_3 - \frac{81}{512}w_4 + \frac{3}{64}w_5 - \frac{3}{512}w_6\right). \tag{11}$$

where the leading truncation error is:

$$\tau_1 = -\frac{1523}{322560}h^6 w_1^{(8)} \tag{12}$$

**Scheme near the Right Boundary ($i = N - 1$):**

$$\begin{aligned} \frac{11}{128}w''_{N-2} + w''_{N-1} + \frac{11}{128}w''_N = \frac{1}{h^2}\Bigg(&-\frac{3}{512}w_{N-6} + \frac{3}{64}w_{N-5} - \frac{81}{512}w_{N-4} + \frac{9}{32}w_{N-3} \\ &+\frac{459}{512}w_{N-2} - \frac{141}{64}w_{N-1} + \frac{585}{512}w_N\Bigg). \end{aligned} \tag{13}$$

where the leading truncation error is:

$$\tau_{N-1} = -\frac{1523}{322560}h^6 w_{N-1}^{(8)} \tag{14}$$

**Scheme at the Right Boundary ($i = N$):**

$$\frac{126}{11}w''_{N-1} + w''_N = \frac{1}{h^2}\left(-\frac{131}{1980}w_{N-6} + \frac{57}{110}w_{N-5} - \frac{18}{11}w_{N-4} + \frac{167}{99}w_{N-3} + \frac{573}{44}w_{N-2} - \frac{2943}{110}w_{N-1} + \frac{13097}{990}w_N\right). \tag{15}$$

where the leading truncation error is:

$$\tau_N = \frac{339}{6160}h^6 w_N^{(8)} \tag{16}$$

### 3.2 Matrix Representation and Operator Construction

The full system of equations, combining interior and boundary schemes, is written in matrix form. The matrices $\mathbf{A}_2$ (LHS coefficients) and $\mathbf{B}_2$ (RHS coefficients) are constructed according to the stencils derived in the previous sections. The spatial differentiation operator matrix, $\mathbf{D}_2$, is then found by solving the linear system:

$$\mathbf{D}_2 = \mathbf{A}_2^{-1}\mathbf{B}_2 \tag{17}$$

where $\mathbf{A}_2$ is an $(N+1) \times (N+1)$ tridiagonal matrix defined as:

$$\mathbf{A}_2 = \begin{bmatrix} 1 & \frac{126}{11} & 0 & 0 & 0 & \dots & 0 \\ \frac{11}{128} & 1 & \frac{11}{128} & 0 & 0 & \dots & 0 \\ 0 & \frac{2}{11} & 1 & \frac{2}{11} & 0 & \dots & 0 \\ \vdots & \ddots & \ddots & \ddots & \ddots & \ddots & \vdots \\ 0 & \dots & 0 & \frac{2}{11} & 1 & \frac{2}{11} & 0 \\ 0 & \dots & 0 & 0 & \frac{11}{128} & 1 & \frac{11}{128} \\ 0 & \dots & 0 & 0 & 0 & \frac{126}{11} & 1 \end{bmatrix}$$

and $\mathbf{B}_2$ is the $(N+1) \times (N+1)$ matrix containing the function weights for the second derivative:

$$\mathbf{B}_2 = \begin{bmatrix} \frac{13097}{990} & -\frac{2943}{110} & \frac{573}{44} & \frac{167}{99} & -\frac{18}{11} & \frac{57}{110} & -\frac{131}{1980} & \dots & 0 \\ \frac{585}{512} & -\frac{141}{64} & \frac{459}{512} & \frac{9}{32} & -\frac{81}{512} & \frac{3}{64} & -\frac{3}{512} & \dots & 0 \\ \frac{3}{44} & \frac{12}{11} & -\frac{51}{22} & \frac{12}{11} & \frac{3}{44} & 0 & 0 & \dots & 0 \\ 0 & \frac{3}{44} & \frac{12}{11} & -\frac{51}{22} & \frac{12}{11} & \frac{3}{44} & 0 & \dots & 0 \\ \vdots & \vdots & \ddots & \ddots & \ddots & \ddots & \ddots & \vdots & \vdots \\ 0 & \dots & 0 & \frac{3}{44} & \frac{12}{11} & -\frac{51}{22} & \frac{12}{11} & \frac{3}{44} & 0 \\ 0 & \dots & -\frac{3}{512} & \frac{3}{64} & -\frac{81}{512} & \frac{9}{32} & \frac{459}{512} & -\frac{141}{64} & \frac{585}{512} \\ 0 & \dots & -\frac{131}{1980} & \frac{57}{110} & -\frac{18}{11} & \frac{167}{99} & \frac{573}{44} & -\frac{2943}{110} & \frac{13097}{990} \end{bmatrix}$$

To solve the system for the unknown interior values while satisfying Dirichlet boundary conditions, we partition $\mathbf{D}_2$ to isolate the contributions from the interior grid points and the boundary nodes.

The interior differentiation matrix, $\mathbf{D}_{2,int} \in \mathbb{R}^{(N-1)\times(N-1)}$, is extracted from the rows and columns corresponding to the interior nodes $i, j \in \{1, 2, \dots, N-1\}$:

$$\mathbf{D}_{2,int} = \mathbf{D}_2(1 : N-1,\, 1 : N-1) \tag{18}$$

The boundary influence matrix, $\mathbf{D}_{2,bound} \in \mathbb{R}^{(N-1)\times 2}$, captures the effect of the prescribed values $w_0$ and $w_N$ on the interior derivatives. It consists of the first and last columns of the interior rows:

$$\mathbf{D}_{2,bound} = \begin{bmatrix} D_{2(1,0)} & D_{2(1,N)} \\ D_{2(2,0)} & D_{2(2,N)} \\ \vdots & \vdots \\ D_{2(N-1,0)} & D_{2(N-1,N)} \end{bmatrix} \tag{19}$$

Using this partitioning, the vector of second derivatives at the interior points, $\mathbf{w}''_{int}(t)$, is calculated as:

$$\mathbf{w}''_{int}(t) = \frac{1}{h^2}\left(\mathbf{D}_{2,int}\mathbf{w}_{int}(t) + \mathbf{D}_{2,bound}\mathbf{w}_{bc}(t)\right) \tag{20}$$

where $\mathbf{w}_{int} = [w_1, w_2, \dots, w_{N-1}]^T$ represents the unknown interior values and $\mathbf{w}_{bc} = [w_0, w_N]^T$ represents the prescribed values at the boundaries.

# 4 Temporal Discretization: Derivation of the Block Collocation Method

To integrate the semi-discrete system (4), we employ a block hybrid collocation method (BHM). The BHM approximates the solution over a time block $[t_n, t_{n+1}]$ with a vector polynomial $\boldsymbol{U}(t)$ constrained to satisfy the differential equation at a set of pre-defined points. Specifically, the method requires that this polynomial matches the solution at the start of the block, $\boldsymbol{U}(t_n) = \boldsymbol{W}_n$, and that its derivative satisfies the ODE system at a set of $m$ distinct collocation points, $t_{n,j} = t_n + p_j h_t$, for $j = 1, \dots, m$:

$$\left.\frac{d\boldsymbol{U}}{dt}\right|_{t=t_{n,j}} = \boldsymbol{G}(t_{n,j}, \boldsymbol{U}(t_{n,j})). \tag{21}$$

To facilitate the derivation, we define a normalized time variable $z = (t - t_n)/h_t \in [0, 1]$, where the collocation points $\{p_j\}_{j=1}^m$ lie in $(0, 1]$.

Since the derivative of the polynomial approximant, $\frac{d\boldsymbol{U}}{dt}$, is itself a polynomial, it can be represented uniquely using Lagrange interpolation over the $m + 1$ points in the set $P = \{p_0, p_1, \ldots, p_m\}$ where $p_0 = 0$. Let $\boldsymbol{G}_k = \boldsymbol{G}(t_{n,k}, \boldsymbol{W}_k)$ be the unknown derivative vector at the $k$-th stage, where $\boldsymbol{W}_k = \boldsymbol{U}(t_{n,k})$. The derivative polynomial is then written as:

$$\frac{d\boldsymbol{U}}{dt}(t_n + zh_t) \approx \sum_{k=0}^{m} \boldsymbol{G}_k L_k(z) \tag{22}$$

where $L_k(z)$ is the $k$-th Lagrange basis polynomial for the set $P$:

$$L_k(z) = \prod_{\substack{j=0 \\ j\neq k}}^{m} \frac{z - p_j}{p_k - p_j}. \tag{23}$$

By the Fundamental Theorem of Calculus, the solution at any point $t$ in the block is given by integrating this derivative from the start of the block:

$$\boldsymbol{W}(t) = \boldsymbol{W}(t_n) + \int_{t_n}^{t} \frac{d\boldsymbol{W}}{ds}(s)\, ds. \tag{24}$$

Applying this to the polynomial approximant at the $j$-th stage point $t_{n,j}$, we change the integration variable to the normalized time $z$ (where $s = t_n + zh_t$ and $ds = h_t dz$) and substitute the Lagrange representation of the derivative:

$$\boldsymbol{W}_{n,j} = \boldsymbol{W}_n + \int_0^{p_j} \left( \sum_{k=0}^{m} \boldsymbol{G}_k L_k(z) \right) h_t\, dz \tag{25}$$

$$= \boldsymbol{W}_n + h_t \sum_{k=0}^{m} \boldsymbol{G}_k \left( \int_0^{p_j} L_k(z)\, dz \right). \tag{26}$$

This leads to the final update formula for each stage $j = 1, \ldots, m$:

$$\boldsymbol{W}_{n,j} = \boldsymbol{W}_n + h_t \sum_{k=0}^{m} \alpha_{jk} \boldsymbol{G}(t_{n,k}, \boldsymbol{W}_{n,k}) \tag{27}$$

where the quadrature coefficients are defined as

$$\alpha_{jk} = \int_0^{p_j} L_k(z)\, dz. \tag{28}$$

Because the stage derivatives $\boldsymbol{G}_k$ depend on the unknown stage solutions $\boldsymbol{W}_{n,k}$, Equation (27) represents a coupled system of nonlinear algebraic equations for the unknown vectors $\{\boldsymbol{W}_{n,1}, \ldots, \boldsymbol{W}_{n,m}\}$. Once the system is solved, the solution at the end of the block is simply $\boldsymbol{W}_{n+1} = \boldsymbol{W}_{n,m}$.

## 5 Solution of the Nonlinear System

To solve system (27) efficiently, we employ Newton's method.

### 5.1 Residual Formulation

Let the stacked vector of unknown stage solutions be defined as

$$\mathbf{W} = \begin{bmatrix} W_{n,1} \\ W_{n,2} \\ \vdots \\ W_{n,m} \end{bmatrix}.$$

We define the residual vector function

$$\mathbf{R}(\mathbf{W}) = \begin{bmatrix} R_1(\mathbf{W}) \\ R_2(\mathbf{W}) \\ \vdots \\ R_m(\mathbf{W}) \end{bmatrix}, \tag{29}$$

where each component is given by

$$R_j(\mathbf{W}) = W_{n,j} - W_n - h_t \sum_{k=0}^{m} \alpha_{jk} G(t_{n,k}, W_{n,k}), \qquad j = 1, \ldots, m. \tag{30}$$

The nonlinear system can therefore be written compactly as

$$\mathbf{R}(\mathbf{W}) = 0. \tag{31}$$

### 5.2 Newton Iteration

Newton's method is applied to solve the nonlinear system iteratively. Given an initial guess $\mathbf{W}^{(0)}$, the Newton iteration computes updates $\Delta\mathbf{W}^{(r)}$ from the linear system

$$J(\mathbf{W}^{(r)})\, \Delta\mathbf{W}^{(r)} = -\mathbf{R}(\mathbf{W}^{(r)}), \tag{32}$$

where

$$J(\mathbf{W}) = \frac{\partial \mathbf{R}}{\partial \mathbf{W}}$$

is the Jacobian matrix of the residual function. The stage vector is then updated according to

$$\mathbf{W}^{(r+1)} = \mathbf{W}^{(r)} + \Delta\mathbf{W}^{(r)}. \tag{33}$$

The iteration is repeated until a prescribed convergence tolerance is satisfied, typically

$$\|\mathbf{R}(\mathbf{W}^{(r)})\| < \varepsilon.$$

### 5.3 Structure of the Jacobian

The Jacobian matrix has a block structure given by

$$J = I - h_t \begin{bmatrix} \alpha_{11} G'_1 & \alpha_{12} G'_2 & \cdots & \alpha_{1m} G'_m \\ \alpha_{21} G'_1 & \alpha_{22} G'_2 & \cdots & \alpha_{2m} G'_m \\ \vdots & \vdots & \ddots & \vdots \\ \alpha_{m1} G'_1 & \alpha_{m2} G'_2 & \cdots & \alpha_{mm} G'_m \end{bmatrix},$$

where

$$G'_k = \frac{\partial G(t_{n,k}, W_{n,k})}{\partial W}.$$

This block structure reflects the coupling between stage solutions introduced by the block hybrid time discretization.

Once the Newton iteration converges, the solution at the end of the time block is obtained from the final stage value

$$W_{n+1} = W_{n,m}. \tag{34}$$

The history term required in the Volterra integral is then updated for the next time block using the quadrature coefficients $\alpha_{mk}$.

# 6 Approximation of the Volterra Integral Term

To evaluate the history-dependent integral $I_i(t) = \int_0^t K(x_i, t, s, w(x_i, s))\, ds$ without re-calculating the entire simulation history at every stage, the integral is partitioned at the start of each time block $[t_n, t_{n+1}]$:

$$I_i(t) = \underbrace{\int_0^{t_n} K(x_i, t, s, w(x_i, s))\, ds}_{\text{History Contribution}} + \underbrace{\int_{t_n}^{t} K(x_i, t, s, w(x_i, s))\, ds}_{\text{Current Block Contribution}} \tag{35}$$

The "History Contribution" is computed using converged values from previous blocks. To maintain high-order accuracy, the "Current Block Contribution" is approximated using the same Lagrange polynomial basis $L_k(z)$ employed for the temporal BHM. For a stage time $t_{n,j}$, the integral is approximated as:

$$\int_{t_n}^{t_{n,j}} K(x_i, t_{n,j}, s, w(x_i, s))\, ds \approx h_t \sum_{k=0}^{m} \alpha_{jk} K(x_i, t_{n,j}, t_{n,k}, W_{i,k}) \tag{36}$$

where $\alpha_{jk} = \int_0^{p_j} L_k(z)\, dz$ are the quadrature weights. This ensures the quadrature error is consistent with the temporal integration error. Upon convergence of the Newton iteration, the history term is updated for the next block using the weights $\alpha_{mk}$.

Substituting the Sixth-Order Compact Finite Difference operator and this consistent quadrature into the Block Hybrid framework yields the final fully discrete scheme for each stage $j = 1, \ldots, m$:

$$\begin{aligned} \boldsymbol{W}_{n,j} = \boldsymbol{W}_n + h_t \sum_{k=0}^{m} \alpha_{jk} \Bigg( & \underbrace{\frac{1}{h^2} \left( \mathbf{D}_{2,\text{int}} \mathbf{W}_{n,k} + \mathbf{D}_{2,\text{bound}} \mathbf{W}_{bc} \right)}_{\text{Spatial CFD}} + \underbrace{\boldsymbol{f}(t_{n,k})}_{\text{Forcing}} \\ & + \underbrace{H(t_{n,k})}_{\text{History Integral}} + \underbrace{h_t \sum_{l=0}^{m} \alpha_{kl} K(t_{n,k}, t_{n,l}, \boldsymbol{W}_{n,l})}_{\text{Current Block Quadrature}} \Bigg) \end{aligned} \tag{37}$$

# 7 Analysis

**Proposition 7.1** (Local Truncation Error)**.** *Let* $\mathbf{W}(t) \in C^{r+2}([t_n, t_{n+1}])$ *be the exact solution of the semi-discrete problem*

$$\mathbf{W}'(t) = \frac{1}{h^2} \left( \mathbf{D}_{2,\text{int}} \mathbf{W}(t) + \mathbf{D}_{2,\text{bound}} \mathbf{W}_{bc} \right) + \boldsymbol{f}(t) + \boldsymbol{H}(t) + \int_{t_n}^{t} \mathcal{K}(t, \tau, \mathbf{W}(\tau))\, d\tau. \tag{38}$$

*Consider the block hybrid scheme*

$$\boldsymbol{W}_{n,j} = \boldsymbol{W}_n + h_t \sum_{k=0}^{m} \alpha_{jk} \left[ \mathcal{F}(t_{n,k}, \boldsymbol{W}_{n,k}) + h_t \sum_{l=0}^{m} \alpha_{kl} \mathcal{K}(t_{n,k}, t_{n,l}, \boldsymbol{W}_{n,l}) \right], \qquad j = 0, \ldots, m, \tag{39}$$

*where*

$$\mathcal{F}(t, \mathbf{W}) = \frac{1}{h^2} \left( \mathbf{D}_{2,\text{int}} \mathbf{W} + \mathbf{D}_{2,\text{bound}} \mathbf{W}_{bc} \right) + \boldsymbol{f}(t) + \text{Hist}(t). \tag{40}$$

*Assume that the block coefficients $\alpha_{jk}$ satisfy the order conditions*

$$\sum_{k=0}^{m} \alpha_{jk} p_k^q = \frac{p_j^{q+1}}{(q+1)!}, \qquad q = 0, 1, \ldots, r, \tag{41}$$

*where $p_j$ are the block nodes in $[0, 1]$. Then the local truncation error at node $t_{n,j}$ is given by*

$$\mathcal{L}_j = \frac{h_t^{r+2}}{(r+2)!} \left[ p_j^{r+2} - (r+2)(r+1) \sum_{k=0}^{m} \alpha_{jk} p_k^{r+1} \right] \mathbf{W}^{(r+2)}(t_n) + \mathcal{O}(h_t^{r+3}), \tag{42}$$

*as $h_t \to 0$. Consequently, the block hybrid time discretization is consistent of order $r + 1$. If, in addition, the compact finite difference operator satisfies*

$$\mathbf{D}_{2,\text{int}} \mathbf{W} = \mathbf{W}_{xx} + \mathcal{O}(h^{\,q}), \tag{43}$$

*then the fully discrete local truncation error satisfies*

$$\mathcal{L}_j = \mathcal{O}(h_t^{r+2}) + \mathcal{O}(h^{\,q}). \tag{44}$$

*Proof.* Let $\mathbf{W}(t)$ denote the exact solution of the semi-discrete problem

$$\mathbf{W}'(t) = \mathcal{F}(t, \mathbf{W}(t)) + \int_{t_n}^{t} \mathcal{K}(t, \tau, \mathbf{W}(\tau))\, d\tau, \tag{45}$$

where

$$\mathcal{F}(t, \mathbf{W}) = \frac{1}{h^2} \left( \mathbf{D}_{2,\text{int}} \mathbf{W} + \mathbf{D}_{2,\text{bound}} \mathbf{W}_{bc} \right) + \boldsymbol{f}(t) + \text{Hist}(t). \tag{46}$$

Expanding $\mathbf{W}(t_{n,j})$ about $t_n$ gives

$$\mathbf{W}(t_{n,j}) = \mathbf{W}(t_n) + p_j h_t \mathbf{W}'(t_n) + \frac{p_j^2 h_t^2}{2!} \mathbf{W}''(t_n) + \cdots + \frac{p_j^{r+2} h_t^{r+2}}{(r+2)!} \mathbf{W}^{(r+2)}(t_n) + \mathcal{O}(h_t^{r+3}). \tag{47}$$

Next, substituting the exact solution into the block hybrid scheme and expanding $\mathcal{F}(t_{n,k}, \mathbf{W}(t_{n,k}))$ about $t_n$, we obtain

$$\mathcal{F}(t_{n,k}, \mathbf{W}(t_{n,k})) = \sum_{q=0}^{r+1} \frac{p_k^q h_t^q}{q!} \mathbf{W}^{(q+1)}(t_n) + \mathcal{O}(h_t^{r+2}). \tag{48}$$

Similarly, for the kernel term,

$$\mathcal{K}(t_{n,k}, t_{n,l}, \mathbf{W}(t_{n,l})) = \sum_{q=0}^{r} \frac{p_l^q h_t^q}{q!} \mathbf{W}^{(q+2)}(t_n) + \mathcal{O}(h_t^{r+1}). \tag{49}$$

Inserting these expansions into the numerical scheme yields a Taylor series in powers of $h_t$. The assumed order conditions

$$\sum_{k=0}^{m} \alpha_{jk} p_k^q = \frac{p_j^{q+1}}{(q+1)!}, \qquad q = 0, 1, \ldots, r, \tag{50}$$

ensure that all terms up to order $h_t^{r+1}$ cancel exactly with the corresponding terms in the Taylor expansion of the exact solution. Consequently, the scheme reproduces the exact Taylor expansion up to degree $r+1$. The first non-vanishing contribution therefore appears at order $h_t^{r+2}$, which gives

$$\mathcal{L}_j = \frac{h_t^{r+2}}{(r+2)!}\left[p_j^{r+2} - (r+2)(r+1)\sum_{k=0}^{m}\alpha_{jk}p_k^{r+1}\right]\mathbf{W}^{(r+2)}(t_n) + \mathcal{O}(h_t^{r+3}). \tag{51}$$

Finally, if the compact finite difference operator satisfies

$$\mathbf{D}_{2,\mathrm{int}}\mathbf{W} = \mathbf{W}_{xx} + \mathcal{O}(h^q), \tag{52}$$

then the spatial discretization contributes an additional term of order $\mathcal{O}(h^q)$. Hence, the fully discrete local truncation error satisfies

$$\mathcal{L}_j = \mathcal{O}(h_t^{r+2}) + \mathcal{O}(h^q), \tag{53}$$

which completes the proof. □

**Theorem 7.1** (Consistency)**.** *Assume that* $\mathbf{W}(t) \in C^{r+2}([t_n, t_{n+1}])$ *and that the block coefficients* $\alpha_{jk}$ *satisfy the order conditions*

$$\sum_{k=0}^{m}\alpha_{jk}p_k^q = \frac{p_j^{q+1}}{(q+1)!}, \qquad q = 0, 1, \ldots, r.$$

*Then the block hybrid time discretization is consistent of order* $r+1$*, i.e.,*

$$\mathcal{L}_j = \mathcal{O}(h_t^{r+2}).$$

*If, in addition, the compact finite difference operator is of spatial order* $q$*, then the fully discrete scheme is consistent with*

$$\mathcal{L}_j = \mathcal{O}(h_t^{r+2}) + \mathcal{O}(h^q).$$

*Proof.* From Proposition 1, the local truncation error satisfies

$$\mathcal{L}_j = \frac{h_t^{r+2}}{(r+2)!}\left[p_j^{r+2} - (r+2)(r+1)\sum_{k=0}^{m}\alpha_{jk}p_k^{r+1}\right]\mathbf{W}^{(r+2)}(t_n) + \mathcal{O}(h_t^{r+3}).$$

Hence,

$$\mathcal{L}_j = \mathcal{O}(h_t^{r+2}).$$

The spatial discretization contributes an additional $\mathcal{O}(h^q)$ term, completing the proof. □

**Theorem 7.2** (Stability)**.** *Assume that*

*(i) The compact finite difference spatial operator satisfies*

$$\|D_{2,int}\| \le Ch^{-2},$$

*(ii) The kernel function* $K(x,t,s,W)$ *is Lipschitz continuous with respect to* $W$*, i.e.,*

$$\|K(x,t,s,W_1) - K(x,t,s,W_2)\| \le L\|W_1 - W_2\|,$$

*(iii) The block coefficient matrix* $A = (\alpha_{jk})$ *generates a bounded evolution operator.*

*Then the fully discrete BHM–CFD scheme is stable. In particular, there exists a constant* $C > 0$ *independent of* $n$ *such that*

$$\|W_n\| \le C\left(\|W_0\| + \max_{0\le k\le n}\|R_k\|\right).$$

*Proof.* The block hybrid time discretization derived in Section 4 can be written in operator form as

$$W_{n+1} = W_n + h_t A G(W_n),$$

where $A = (\alpha_{jk})$ is the block coefficient matrix and $G(W_n)$ contains the spatial discretization and Volterra integral terms. Separating the spatial operator and forcing terms gives

$$W_{n+1} = (I + h_t A L_h) W_n + h_t A R_n,$$

where

$$L_h = D_{2,int}$$

denotes the compact finite difference spatial operator and $R_n$ contains the kernel and source contributions. Taking norms on both sides yields

$$\|W_{n+1}\| \leq \|(I + h_t A L_h)\| \, \|W_n\| + h_t \|A\| \|R_n\|.$$

Using the submultiplicative property of matrix norms,

$$\|(I + h_t A L_h)\| \leq 1 + h_t \|A\| \|L_h\|.$$

From assumption (i),

$$\|L_h\| \leq C h^{-2}.$$

Hence,

$$\|W_{n+1}\| \leq (1 + C h_t) \|W_n\| + C h_t \|R_n\|.$$

This inequality defines a discrete recursive bound. Applying the discrete Gronwall inequality gives

$$\|W_n\| \leq C \left( \|W_0\| + \max_{0 \leq k \leq n} \|R_k\| \right),$$

where the constant $C$ is independent of $n$. Therefore the numerical solution remains bounded for all time steps, which establishes the stability of the BHM–CFD scheme. □

**Theorem 7.3** (Convergence)**.** *Suppose the scheme is consistent of order $r+1$ and stable in the sense of Theorem 2. Then the fully discrete solution satisfies*

$$\|\mathbf{W}_n - \mathbf{W}(t_n)\| \leq C \left( h_t^{r+1} + h^q \right),$$

*for $0 \leq t_n \leq T$. Hence the method is convergent of order* $\min(r+1, q)$.

*Proof.* Let $\mathbf{e}_n = \mathbf{W}_n - \mathbf{W}(t_n)$. Subtracting the numerical scheme from the exact equation gives

$$\mathbf{e}_{n+1} = \mathcal{M} \mathbf{e}_n + \boldsymbol{\tau}_n,$$

where $\boldsymbol{\tau}_n$ is the local truncation error. From consistency,

$$\|\boldsymbol{\tau}_n\| \leq C(h_t^{r+2} + h^q).$$

Using stability and discrete Gronwall inequality,

$$\|\mathbf{e}_n\| \leq C \max_{k \leq n} \|\boldsymbol{\tau}_k\|.$$

Therefore,

$$\|\mathbf{e}_n\| \leq C(h_t^{r+1} + h^q),$$

which completes the proof. □

# 8 Numerical Experiments

In this section, several numerical experiments are presented to examine the performance, accuracy, and efficiency of the proposed Block Hybrid Compact Finite Difference (BHM–CFD) scheme. The method is applied to representative test problems with known analytical solutions, which enables a direct assessment of the numerical errors. For each problem, the maximum absolute error

$$\|E\|_\infty = \max_{i,j} |w(x_i, t_j) - W_{i,j}|$$

is computed to evaluate the accuracy of the numerical approximation. The results obtained using the proposed method are compared with those reported in the literature in order to demonstrate its effectiveness and improved accuracy.

**Example 8.1.** *Consider the linear PVIDE defined as:*

$$\frac{\partial w}{\partial t} - \frac{\partial^2 w}{\partial x^2} + \int_0^t e^{x(t-s)} w(x,s)\, ds = g(x,t) \tag{54}$$

*subject to the initial and boundary conditions:*

$$w(x,0) = 0, \quad w(0,t) = \sin(t), \quad w(1,t) = 0 \tag{55}$$

*where $g(x,t)$ is the source term corresponding to the exact analytical solution $w(x,t) = (1-x^2)\sin(t)$:*

$$g(x,t) = \frac{(1-x^2)e^{xt} + (x^3 + 2x^2 - x + 2)\sin(t) + (x^2 - x^4)\cos(t)}{x^2 + 1} \tag{56}$$

Table 1: Comparison of maximum absolute error ($\|E\|_\infty$) for Example 8.1

| **Method** | $\|E\|_\infty$ | **Method** | $\|E\|_\infty$ |
|---|---|---|---|
| BHM-CFD (proposed) ($N_t = 16$) | $3.200 \times 10^{-13}$ | Rostamy & Mirzaei [22] ($N = 20$) | $1.9900 \times 10^{-7}$ |
| Mirzahashemi & Heydari [20] ($\Delta t = 0.001$) | $1.7293 \times 10^{-12}$ | Aziz and Khan [23] | $6.6396 \times 10^{-5}$ |
| Zeghdane [21] ($N = 8$) | $2.5266 \times 10^{-10}$ | FM-DQM ($\Delta t = 0.001$) | $6.4554 \times 10^{-4}$ |
| Tchier et al. [4] ($N = 10$) | $3.8785 \times 10^{-10}$ | | |

Table 2: Temporal convergence rates for Example 8.1 with varying $N_t$.

| $N_t$ | $\|\|E\|\|_\infty$ | ROC |
|---|---|---|
| 1 | $2.03443 \times 10^{-6}$ | – |
| 2 | $4.34604 \times 10^{-8}$ | 5.55 |
| 4 | $7.52154 \times 10^{-10}$ | 5.85 |
| 8 | $1.21994 \times 10^{-11}$ | 5.95 |
| 16 | $2.08722 \times 10^{-13}$ | 5.87 |

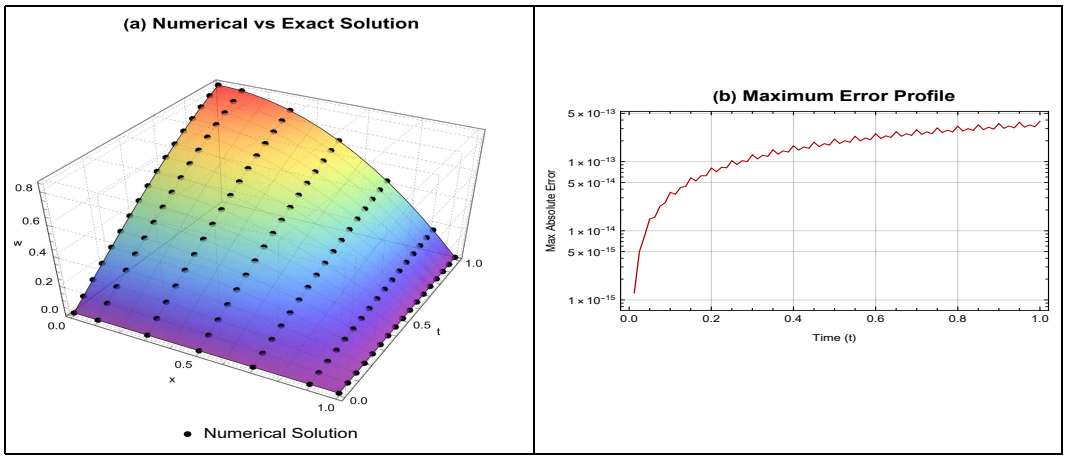



Figure 1: Numerical performance of the BHM-CFD scheme for Example 8.1.

A comparison of the numerical results of Example 8.1 with several other methods is presented in Table 1. The table shows that the proposed BHM–CFD scheme attains a maximum absolute error of $3.2\times10^{-13}$, which is significantly smaller than those reported by the competing methods.

The temporal convergence results in Table 2 indicate a consistent rate approaching six as $N_t$ increases, confirming the theoretical sixth-order temporal accuracy of the scheme. The error decreases monotonically and approaches machine precision for finer discretizations, with no evidence of order degradation. Figure 1 further confirms the accuracy of the method, as the numerical solution is visually indistinguishable from the exact solution over the entire domain. These results demonstrate that the proposed BHM–CFD scheme provides highly accurate, stable, and sixth-order convergent solutions for the problem under consideration.

**Example 8.2.** *Consider the nonlinear PVIDE defined as:*

$$\frac{\partial w}{\partial t} + \frac{\partial^2 w}{\partial x^2} = \int_0^t e^{x+t+s} w^2(x,s)\, ds + g(x,t) \tag{57}$$

*subject to the initial and boundary conditions:*

$$w(x,0) = x, \quad w(0,t) = 0, \quad w(1,t) = \cos(t) \tag{58}$$

*The source term $g(x,t)$ corresponding to the exact solution $w(x,t) = x\cos(t)$ is given by:*

$$g(x,t) = -x\sin(t) - \frac{x^2}{5}\left[e^{x+2t}(\cos^2(t) + \sin(2t) + 2) - 3e^{x+t}\right] \tag{59}$$

The numerical results for Example 8.2, shown in Table 3 and Fig. 2, demonstrate the superior performance of the BHM-CFD scheme compared to existing approaches. The method achieves significantly higher precision while maintaining a robust sixth-order convergence rate with exceptional computational efficiency. As shown in Figure 2(a), the numerical solution aligns perfectly with the exact surface, while Figure 2(b) indicates that the absolute error remains stable and bounded across the temporal domain. Furthermore, the efficiency of the quasilinearization approach is highlighted in Figure 2(c), where the residuals drop rapidly to a stable floor within just a few iterations, confirming the method's robustness for this class of problems.

**Example 8.3.** *Consider the nonlinear PVIDE defined as:*

$$\frac{\partial w}{\partial t} = (1+x^2)\frac{\partial^2 w}{\partial x^2} + t\int_0^t [w(x,s)]^2\, ds + x^2 t + g(x,t) \tag{60}$$

Table 3: Comparison of errors for Example 8.2.

| | **Tchier et al [4]** | **BHM-CFD** (Proposed method) | | |
|---|---|---|---|---|
| $N_t$ | $\|E\|_\infty$ | $\|E\|_\infty$ | **ROC** | **CPU(s)** |
| 2 | $3.8674 \times 10^{-1}$ | $6.45 \times 10^{-7}$ | – | 0.25 |
| 3 | $2.9204 \times 10^{-2}$ | $5.42 \times 10^{-8}$ | 6.11 | 0.24 |
| 4 | $7.7564 \times 10^{-3}$ | $9.28 \times 10^{-9}$ | 6.14 | 0.27 |
| 5 | $2.6865 \times 10^{-4}$ | $2.37 \times 10^{-9}$ | 6.11 | 0.36 |
| 6 | $3.9205 \times 10^{-5}$ | $7.82 \times 10^{-10}$ | 6.09 | 0.38 |
| 7 | $6.2192 \times 10^{-6}$ | $3.07 \times 10^{-10}$ | 6.07 | 0.44 |
| 8 | $4.8173 \times 10^{-7}$ | $1.37 \times 10^{-10}$ | 6.05 | 0.45 |

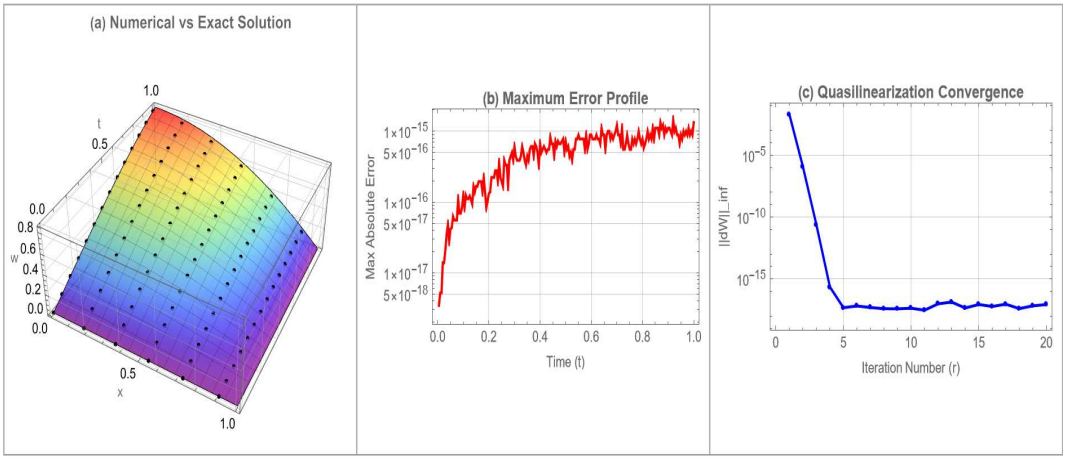



Figure 2: Numerical performance of the BHM-CFD scheme for Example 8.2.

*The source term $g(x,t)$ is analytically derived to force the exact solution $w(x,t) = \sinh(x) + e^{-xt}$:*

$$\begin{aligned} g(x,t) = &- xe^{-xt} - (1+x^2)(\sinh(x) + t^2 e^{-xt}) - x^2 t \\ &- t\left[t\sinh^2(x) - \frac{2\sinh(x)}{x}(e^{-xt} - 1) - \frac{1}{2x}(e^{-2xt} - 1)\right] \end{aligned} \tag{61}$$

*The initial condition at $t = 0$ is:*

$$w(x,0) = \sinh(x) + 1 \tag{62}$$

*The time-dependent Dirichlet boundary conditions on the domain $x \in [0,1]$ are:*

$$\begin{cases} w(0,t) = 1 \\ w(1,t) = \sinh(1) + e^{-t} \end{cases} \tag{63}$$

*The problem is constructed such that the analytical solution is:*

$$w(x,t) = \sinh(x) + e^{-xt} \tag{64}$$

The numerical results for Example 8.3 demonstrate the high accuracy and computational efficiency of the proposed BHM-CFD scheme.

Table 4: Numerical results for Example 8.3

| **Method** | $N_t$ | $L_\infty$ **Error** | **ROC** ($L_\infty$) | $L_2$ **Error** | **ROC** ($L_2$) |
|---|---|---|---|---|---|
| Avazzadeh et al. [5] | — | $3.1977 \times 10^{-4}$ | — | $6.9050 \times 10^{-5}$ | — |
| BHM-CFD (Proposed Method) | 2 | $1.58 \times 10^{-8}$ | — | $8.88 \times 10^{-9}$ | — |
| | 3 | $1.64 \times 10^{-9}$ | 5.58 | $8.31 \times 10^{-10}$ | 5.84 |
| | 4 | $3.33 \times 10^{-10}$ | 5.54 | $1.52 \times 10^{-10}$ | 5.91 |
| | 5 | $9.73 \times 10^{-11}$ | 5.51 | $4.05 \times 10^{-11}$ | 5.92 |
| | 6 | $3.54 \times 10^{-11}$ | 5.54 | $1.39 \times 10^{-11}$ | 5.88 |
| | 7 | $1.52 \times 10^{-11}$ | 5.51 | $5.74 \times 10^{-12}$ | 5.72 |
| | 8 | $7.37 \times 10^{-12}$ | 5.40 | $2.79 \times 10^{-12}$ | 5.39 |

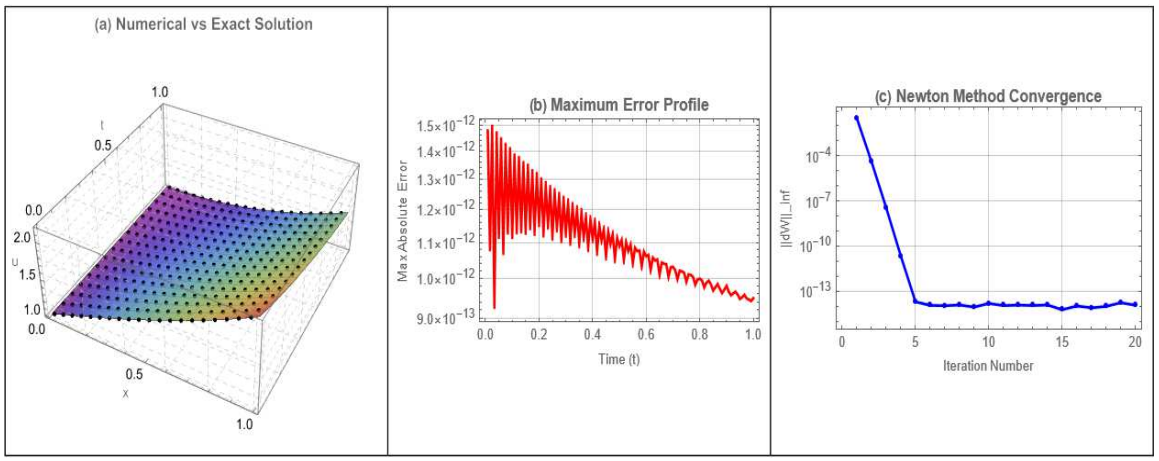



Figure 3: Numerical performance of the BHM-CFD scheme for Example 8.3

As shown in Table 4, the method achieves an $L_\infty$ error of $1.58 \times 10^{-8}$ with only $N_t = 2$, significantly outperforming the $3.1977 \times 10^{-4}$ reported in previous literature. As the discretization is refined to $N_t = 8$, the accuracy improves to the $10^{-12}$ level, maintaining a consistent convergence order (ROC) of about 5.5, which confirms the high-order nature of the solver. This performance is further supported by Figure 3(a), where the numerical points perfectly align with the exact solution surface, and Figure 3(b), which shows that the maximum absolute error remains stable and bounded over the entire temporal domain. Furthermore, the quasilinearization approach proves highly robust, as evidenced by Figure 3(c), where the Newton iteration residual drops to machine precision ($\approx 10^{-14}$) within just five iterations, highlighting the quadratic convergence and reliability of the method for solving complex nonlinear PVIDEs.

**Example 8.4.** *Consider the nonlinear PVIDE defined as:*

$$\frac{\partial w}{\partial t} = \frac{x^2}{2}\frac{\partial^2 w}{\partial x^2} + \int_0^t (1-2x)e^{s-2t}[w(x,s)]^3\, ds + g(x,t) \tag{65}$$

*The source term $g(x,t)$ is analytically derived to force the exact solution $w(x,t) = -x^3 e^{-x^2 t}$:*

$$g(x,t) = (x^5 + 3x^3 - 7x^5 t + 2x^7 t^2)e^{-x^2 t} - \frac{(2x-1)x^9(e^{-t-3x^2 t} - e^{-2t})}{1-3x^2} \tag{66}$$

*The initial condition at $t = 0$ is:*

$$w(x,0) = -x^3 \tag{67}$$

*The time-dependent Dirichlet boundary conditions on the domain $x \in [0,1]$ are:*

$$\begin{cases} w(0,t) = 0 \\ w(1,t) = -e^{-t} \end{cases} \tag{68}$$

*The problem is constructed such that the analytical solution is:*

$$w(x,t) = -x^3 e^{-x^2 t} \tag{69}$$

Table 5: Numerical results for Example 8.4.

| **Method** | $N_t$ | $L_\infty$ **Error** | **ROC** ($L_\infty$) | $L_2$ **Error** | **ROC** ($L_2$) |
|---|---|---|---|---|---|
| Avazzadeh et al [5] | — | $1.2075 \times 10^{-5}$ | — | $5.4369 \times 10^{-5}$ | — |
| BHM-CFD (Proposed Method) | 2 | $8.54 \times 10^{-9}$ | — | $2.69 \times 10^{-9}$ | — |
| | 4 | $2.33 \times 10^{-10}$ | 5.20 | $5.89 \times 10^{-11}$ | 5.51 |
| | 8 | $5.57 \times 10^{-12}$ | 5.39 | $1.06 \times 10^{-12}$ | 5.80 |
| | 16 | $1.37 \times 10^{-13}$ | 5.35 | $4.61 \times 10^{-14}$ | 4.52 |

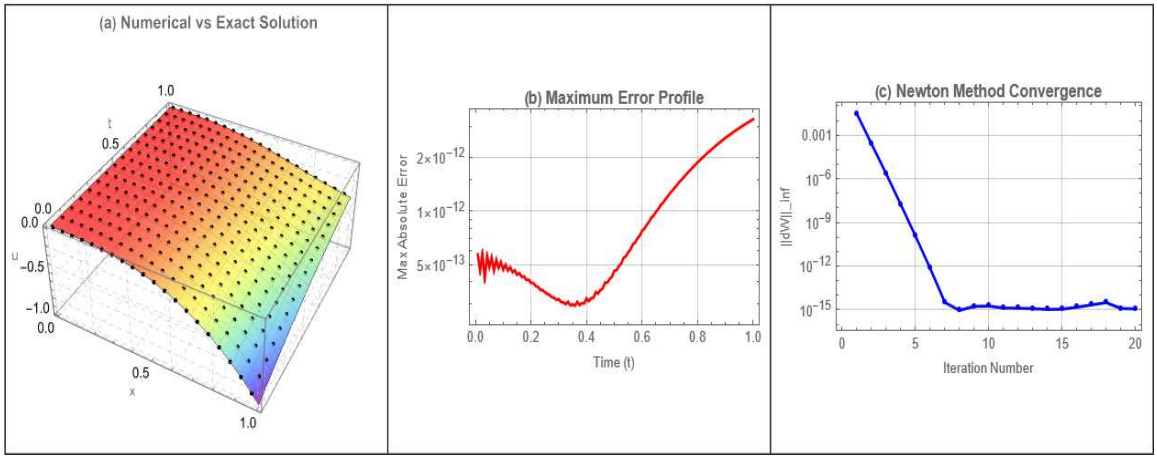



Figure 4: Numerical performance of the BHM-CFD scheme for Example 8.4

The numerical results for Example 8.4 shown in Table 5 and Figure 4, confirm the high-order accuracy and efficiency of the BHM-CFD scheme. The method significantly outperforms existing benchmarks, maintaining a consistent convergence rate as errors approach machine precision. As shown in Figure 4(a), the numerical solution aligns perfectly with the exact surface, while Figure 4(b) demonstrates a stable and bounded error profile across the temporal domain. Furthermore, Figure 4(c) highlights the rapid quadratic convergence of the Newton method, underscoring the solver's robustness for nonlinear PVIDEs.

**Example 8.5.** *Consider the nonlinear PVIDE defined as:*

$$\frac{\partial w}{\partial t} = (x^5 + 4x^2)\frac{\partial^2 w}{\partial x^2} + \int_0^t (x^3 t^3 + 1) s^2 [w(x,s)]^4 \, ds + g(x,t) \tag{70}$$

*The source term $g(x,t)$ is analytically derived to force the exact solution $w(x,t) = e^{-t}\sin(x)$:*

$$g(x,t) = (x^5 + 4x^2 - 1)e^{-t}\sin(x) - \frac{x^3 t^3 + 1}{32}\sin^4(x)\left[1 - e^{-4t}(8t^2 + 4t + 1)\right] \tag{71}$$

*The initial condition at $t = 0$ is:*

$$w(x, 0) = \sin(x) \tag{72}$$

*The time-dependent Dirichlet boundary conditions are:*

$$\begin{cases} w(0, t) = 0 \\ w(1, t) = e^{-t} \sin(1) \end{cases} \tag{73}$$

*The problem is constructed such that the analytical solution is:*

$$w(x, t) = e^{-t} \sin(x) \tag{74}$$

Table 6: Numerical results for Example 8.5

| **Method** | $N_t$ | $L_\infty$ **Error** | **ROC** ($L_\infty$) | $L_2$ **Error** | **ROC** ($L_2$) |
|---|---|---|---|---|---|
| Avazzadeh et al [5] | — | $1.2075 \times 10^{-5}$ | — | $5.4369 \times 10^{-5}$ | — |
| BHM-CFD (Proposed Method) | 1 | $4.2100 \times 10^{-6}$ | — | $2.9300 \times 10^{-6}$ | — |
| | 2 | $1.5900 \times 10^{-7}$ | 4.73 | $6.4300 \times 10^{-8}$ | 5.51 |
| | 4 | $3.9600 \times 10^{-9}$ | 5.32 | $1.0900 \times 10^{-9}$ | 5.88 |
| | 8 | $7.2400 \times 10^{-11}$ | 5.77 | $1.7600 \times 10^{-11}$ | 5.95 |
| | 16 | $1.3900 \times 10^{-12}$ | 5.71 | $4.1100 \times 10^{-13}$ | 5.42 |

The numerical results for Example 8.5 in Table 6 and Figure 5) further illustrate the superior performance of the BHM-CFD scheme. The method achieves high-order precision, outperforming benchmark results even at the lowest temporal resolution while maintaining a near-sixth-order convergence rate. In Figure 5(a), the numerical solution points perfectly capture the exact surface, while the error profile in Figure 5(b) remains extremely small and well-controlled over the entire time interval. Furthermore, the rapid reduction of the residual to machine precision within just a few iterations, shown in Figure 5(c), highlights the efficiency and quadratic convergence of the quasilinearization approach for this problem.

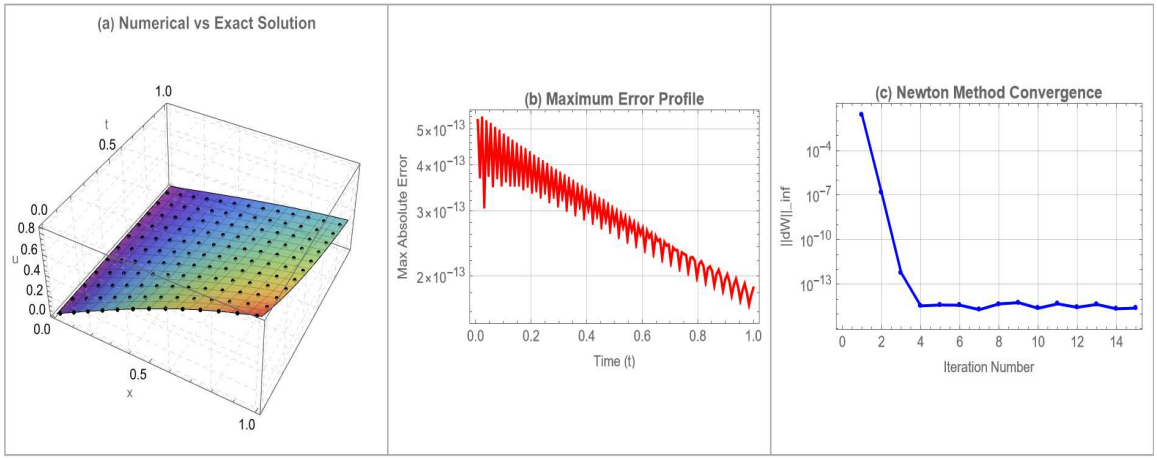



Figure 5: Numerical performance of the BHM-CFD scheme for Example 8.5

**Example 8.6.** *Consider the nonlinear PVIDE with an exponential kernel:*

$$\frac{\partial w}{\partial t} = (x^3 + 1)\frac{\partial^2 w}{\partial x^2} + 3tx^2 \int_0^t s^2 e^{w(x,s)}\, ds + g(x, t) \tag{75}$$

*where* $x \in [0,1]$ *and* $t \in [0,1]$. *The source term* $g(x,t)$ *is analytically derived to force the exact solution* $w(x,t) = \frac{1}{3}x^3t^3$*:*

$$g(x,t) = x^3t^2 - 2xt^3(x^3+1) - \frac{3t}{x}\left(e^{\frac{1}{3}x^3t^3} - 1\right) \tag{76}$$

*The initial condition at* $t = 0$ *is:*

$$w(x,0) = 0 \tag{77}$$

*The time-dependent Dirichlet boundary conditions are:*

$$\begin{cases} w(0,t) = 0 \\ w(1,t) = \frac{1}{3}t^3 \end{cases} \tag{78}$$

*The problem is constructed such that the analytical solution is:*

$$w(x,t) = \frac{1}{3}x^3t^3 \tag{79}$$

Table 7: Numerical results for Example 8.6

| **Method** | $N_t$ | $L_\infty$ **Error** | **Order** $(L_\infty)$ | $L_2$ **Error** | **Order** $(L_2)$ |
|---|---|---|---|---|---|
| Avazzadeh et al [5] | — | $2.0783 \times 10^{-4}$ | — | $9.4007 \times 10^{-4}$ | — |
| Proposed Method | 1 | $5.5400 \times 10^{-6}$ | — | $1.9100 \times 10^{-6}$ | — |
| | 2 | $1.8500 \times 10^{-7}$ | 4.91 | $1.0300 \times 10^{-7}$ | 4.22 |
| | 4 | $4.4100 \times 10^{-9}$ | 5.39 | $2.8500 \times 10^{-9}$ | 5.17 |
| | 8 | $9.0400 \times 10^{-11}$ | 5.61 | $5.6700 \times 10^{-11}$ | 5.65 |
| | 16 | $1.4700 \times 10^{-12}$ | 5.94 | $9.1000 \times 10^{-13}$ | 5.96 |
| | 32 | $1.1300 \times 10^{-13}$ | 3.71 | $4.7600 \times 10^{-14}$ | 4.26 |

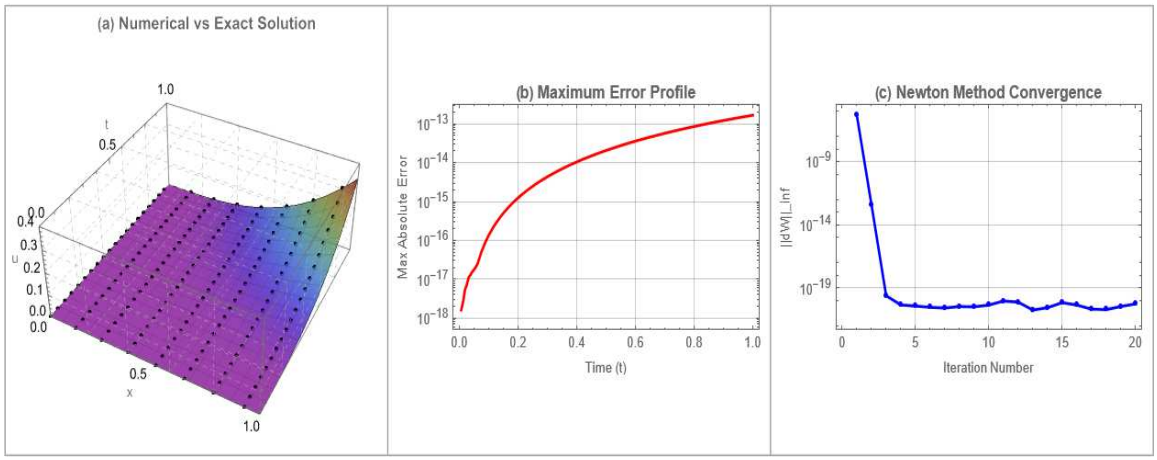



Figure 6: Numerical performance of the BHM-CFD scheme for Example 8.6.

The numerical results for Example 8.6, shown in Table 7 and Figure 6, demonstrate the sustained high-order accuracy and efficiency of the BHM-CFD scheme. The method yields significantly smaller errors compared to existing benchmark results, reaching near-machine precision as the temporal grid is refined. As shown in Figure 6(a), the numerical points coincide perfectly with the exact solution surface. Figure 6(b) illustrates that the maximum absolute error remains bounded and remarkably low throughout the entire time interval. Furthermore,

Figure 6(c) highlights the exceptional efficiency of the quasilinearization approach, which converges to machine precision in only three iterations, confirming the robustness of the solver for nonlinear problems.

**Example 8.7.** *Consider the PVIDE defined as:*

$$\frac{\partial w}{\partial t} = a(x)\frac{\partial^2 w}{\partial x^2} + e^{x+t}\int_0^t e^s[w(x,s)]^2\,ds + g(x,t) \tag{80}$$

*where* $x \in [0,1]$ *and* $t \in [0,1]$. *The diffusion coefficient is given by:*

$$a(x) = \cos^2(x) + \sin(x) \tag{81}$$

*The source term* $g(x,t)$ *is analytically derived to satisfy the exact solution* $w(x,t) = x\cos(t)$*:*

$$g(x,t) = -x\sin(t) - \frac{x^2 e^{x+t}}{10}\left[e^t(5+\cos(2t)+2\sin(2t)) - 6\right] \tag{82}$$

*The initial condition at* $t = 0$ *is:*

$$w(x,0) = x \tag{83}$$

*The time-dependent Dirichlet boundary conditions are:*

$$\begin{cases} w(0,t) = 0 \\ w(1,t) = \cos(t) \end{cases} \tag{84}$$

*The problem is constructed such that the analytical solution is:*

$$w(x,t) = x\cos(t) \tag{85}$$

Table 8: Numerical results for Example 8.7

| **Method** | $N_t$ / $\delta t$ | $L_\infty$ **Error** | **Order** ($L_\infty$) | $L_2$ **Error** | **Order** ($L_2$) |
|---|---|---|---|---|---|
| Avazzadeh et al [5] | $\delta t = 10^{-3}$ | $2.4780 \times 10^{-7}$ | — | $5.0876 \times 10^{-7}$ | — |
| | $\delta t = 10^{-4}$ | $2.5000 \times 10^{-9}$ | — | $5.0628 \times 10^{-9}$ | — |
| Proposed Method | 1 | $2.8000 \times 10^{-5}$ | — | $1.9700 \times 10^{-5}$ | — |
| | 2 | $6.2900 \times 10^{-7}$ | 5.48 | $4.3400 \times 10^{-7}$ | 5.50 |
| | 4 | $7.5700 \times 10^{-9}$ | 6.38 | $5.2900 \times 10^{-9}$ | 6.36 |
| | 8 | $1.0800 \times 10^{-10}$ | 6.13 | $7.5900 \times 10^{-11}$ | 6.12 |
| | 16 | $1.2900 \times 10^{-12}$ | 6.38 | $8.9000 \times 10^{-13}$ | 6.41 |

The numerical results for Example 8.7 shown in Table 8 and Figure 7), confirm the superior accuracy and efficiency of the proposed BHM-CFD scheme. The method significantly outperforms existing literature, maintaining a consistent sixth-order convergence rate as errors reach the $10^{-13}$ level. As illustrated in Figure 7(a), the numerical solution aligns precisely with the exact surface. Figure 7(b) shows that the maximum absolute error remains bounded and remarkably low across the entire time domain. Additionally, the rapid reduction of the residual to machine precision in Figure 7(c) demonstrates the robustness and quadratic convergence of the quasilinearization approach for this nonlinear problem.

**Example 8.8.** *Consider the PVIDE defined as:*

$$\frac{\partial w}{\partial t} = \frac{\partial^2 w}{\partial x^2} + \int_0^t w(x,s)\,ds + g(x,t) \tag{86}$$

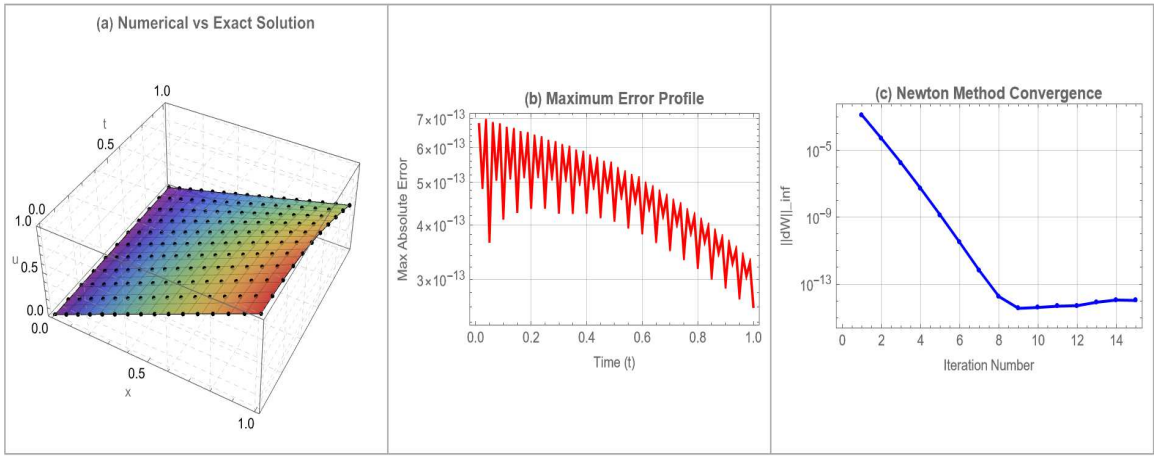



Figure 7: Numerical performance of the BHM-CFD scheme for Example 8.7.

*The source term $g(x,t)$ is analytically derived to force the exact solution $w(x,t) = (1-x^6)\sin(x+t)$:*

$$g(x,t) = \left[2(1-x^6) + 12x^5\right]\cos(x+t) + \left(1 + 30x^4 - x^6\right)\sin(x+t) - (1-x^6)\cos(x) \tag{87}$$

*The initial condition at $t = 0$ is:*

$$w(x,0) = (1-x^6)\sin(x) \tag{88}$$

*The time-dependent homogeneous Dirichlet boundary conditions on the domain $x \in [-1,1]$ are:*

$$\begin{cases} w(-1,t) = 0 \\ w(1,t) = 0 \end{cases} \tag{89}$$

*The problem is constructed such that the analytical solution is:*

$$w(x,t) = (1-x^6)\sin(x+t) \tag{90}$$

Table 9: Numerical results for Example 8.8 ($N_x = 200$)

| $N_t$ | $L_\infty$ | ROC($L_\infty$) | $L_2$ Error | ROC($L_2$) |
|---|---|---|---|---|
| 1 | $4.05 \times 10^{-6}$ | – | $3.75 \times 10^{-6}$ | – |
| 2 | $6.08 \times 10^{-8}$ | 6.06 | $6.05 \times 10^{-8}$ | 5.95 |
| 4 | $9.16 \times 10^{-10}$ | 6.05 | $9.39 \times 10^{-10}$ | 6.01 |
| 8 | $1.29 \times 10^{-11}$ | 6.15 | $1.32 \times 10^{-11}$ | 6.15 |

The numerical results for Example 8.8 shown in Table 9 and Fig. 8, highlight the high-order accuracy and computational efficiency of the BHM-CFD scheme. The method maintains a consistent sixth-order convergence rate, with errors decaying rapidly toward machine precision as the temporal grid is refined. As shown in Figure 8(a), the numerical solution points are in excellent agreement with the exact surface. Figure 8(b) demonstrates that the maximum absolute error remains remarkably small and stable across the entire time interval. Furthermore, the rapid reduction of the residual to machine precision in Figure 8(c) underscores the robustness and quadratic convergence of the solver for this problem across spatial domains.

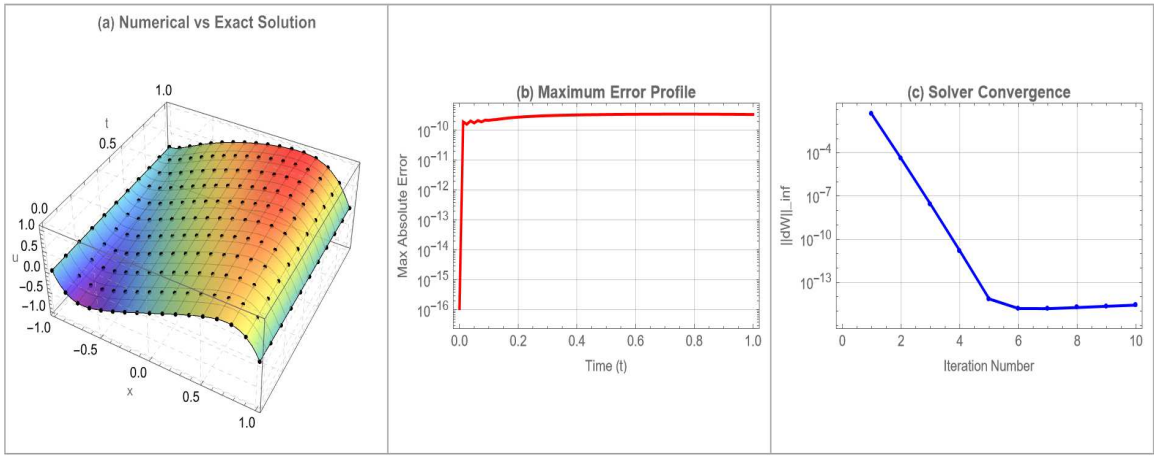



Figure 8: Numerical performance of the BHM-CFD scheme for Example 8.8.

# 9 Conclusion

This work introduces a BHM–CFD scheme for solving nonlinear parabolic Volterra partial integro-differential equations. The method is constructed within the Method of Lines (MOL) framework, using a sixth-order implicit compact finite-difference scheme for spatial discretization and a high-order block-hybrid method for time integration. To handle the Volterra integral term, a consistent quadrature-marching strategy based on the same Lagrange polynomial basis as the time discretization is employed, thereby retaining sixth-order accuracy.

The method is tested on a variety of problems, including linear cases and those with exponential nonlinearities and nonlinear kernels. The numerical results demonstrate that the scheme is highly accurate and compares favorably with existing approaches, achieving maximum absolute errors on the order of $10^{-13}$.

# Declarations


- **Funding:** The authors received no financial support for the research.
- **Competing Interests:** The authors declare that they have no competing interests.


# References


[1] F. Fakhar-Izadi and M. Dehghan, *Fully spectral collocation method for nonlinear parabolic partial integro-differential equations*, Appl. Numer. Math., vol. 123, pp. 99–120, 2018.

[2] M. Sameeh and A. Elsaid, *Chebyshev collocation method for parabolic partial integro-differential equations*, Adv. Math. Phys., vol. 2016, Art. ID 7854806, 2016.

[3] M. Uddin, N. Ullah, and S. I. A. Shah, *RBF-based localized method for solving nonlinear partial integro-differential equations*, Comput. Model. Eng. Sci., vol. 123, no. 3, pp. 957–972, 2020.

[4] F. Tchier, I. Dassios, F. Tawfiq, and L. Ragoub, *On the approximate solution of partial integro-differential equations using the pseudospectral method based on Chebyshev cardinal functions*, Mathematics, vol. 9, Art. 286, 2021.

[5] Z. Avazzadeh, Z. Beygi Rizi, F. M. Maalek Ghaini, and G. B. Loghmani, *A semi-discrete scheme for solving nonlinear hyperbolic-type partial integro-differential equations using radial basis functions*, J. Math. Phys., vol. 52, Art. 063520, 2011.

[6] N. A. Mohammad, Y. A. Sabawi, and M. Sh. Hasso, *Numerical solution based on the Haar wavelet collocation method for partial integro-differential equations of Volterra type*, Arab J. Basic Appl. Sci., vol. 31, no. 1, pp. 614–628, 2024.

[7] P. G. Dlamini, S. S. Motsa, and M. Khumalo, *On the comparison between compact finite difference and pseudospectral approaches for solving similarity boundary layer problems*, Math. Probl. Eng., vol. 2013, Art. ID 2013, 2013.

[8] J. N. Kouagou, P. G. Dlamini, and S. M. Simelane, *On the multi-domain compact finite difference relaxation method for high-dimensional chaos: the nine-dimensional Lorenz system*, Alexandria Eng. J., vol. 59, pp. 2617–2625, 2020.

[9] J. Malele, P. Dlamini, and S. Simelane, *Solving Lane–Emden equations with boundary conditions of various types using high-order compact finite differences*, Appl. Math. Sci. Eng., vol. 31, no. 1, 2023.

[10] J. Malele, P. Dlamini, and S. Simelane, *Highly accurate compact finite difference schemes for two-point boundary value problems with Robin boundary conditions*, Symmetry, vol. 14, Art. 1720, 2022.

[11] P. G. Dlamini and M. Khumalo, *A new compact finite difference quasilinearization method for nonlinear evolution partial differential equations*, Open Math., vol. 15, pp. 1450–1462, 2017.

[12] D. Mathale, P. G. Dlamini, and M. Khumalo, *Compact finite difference relaxation method for chaotic and hyperchaotic initial value systems*, Comput. Appl. Math., vol. 37, pp. 5187–5202, 2018.

[13] P. Dlamini, J. Malele, and S. Simelane, *Solving singular boundary value problems using higher-order compact finite difference schemes with a novel higher-order implementation of Robin boundary conditions*, J. Math. Chem., vol. 61, pp. 1604–1632, 2023.

[14] I. M. Dibal and Y. S. Hoe, *Fifth-order block hybrid approach for solving first-order stiff ordinary differential equations*, Appl. Math., 2026.

[15] S. Shateyi, *On the application of block hybrid methods to solve linear and nonlinear first-order differential equations*, Axioms, 2023.

[16] O. A. Akinfenwa et al., *Seventh-order hybrid block method for solution of first-order stiff systems of initial value problems*, J. Egypt. Math. Soc., 2020.

[17] S. A. A. Ahmedai Abd Allah et al., *A block hybrid method with equally spaced grid points for third-order initial value problems*, Appl. Math., 2024.

[18] S. Motsa et al., *A rational optimal block hybrid method for enhanced accuracy in solving Lane–Emden equations*, Partial Differ. Equ. Appl. Math., 2024.

[19] M. Bisheh-Niasar et al., *An optimized hybrid block method for solving nonlinear singularly perturbed problems using non-uniform Jain-type meshes*, Int. J. Comput. Math., 2024.

[20] R. Mirzahashemi and M. Heydari, *Two modified cubic B-spline differential quadrature methods for solving one- and two-dimensional parabolic Volterra partial integro-differential equations*, Comput. Appl. Math., vol. 45, Art. 160, 2025.

[21] R. Zeghdane, *New adaptive numerical algorithm for solving partial integro-differential equations*, Qeios, 2023.

[22] D. Rostamy and F. Mirzaei, *A class of developed schemes for parabolic integro-differential equations*, Int. J. Comput. Math., vol. 98, no. 12, pp. 2482–2503, 2021.

[23] I. Aziz and I. Khan, *Numerical solution of partial integro-differential equations of diffusion type*, Math. Probl. Eng., vol. 2017, Art. ID 2853679, 2017.